Dendritic upconverting nanoparticles enable in vivo multiphoton microscopy with low-power continuous wave sources

Tatiana V. Esipova[a], Xingchen Ye[b], Joshua E. Collins[c], Sava Sakadžić[d], Emiri T. Mandeville[e], Christopher B. Murray[b,f,1], and Sergei A. Vinogradov[a,1]

Departments of [a]Biochemistry and Biophysics, [b]Chemistry, and [f]Material Science, University of Pennsylvania, Philadelphia, PA 19104; [c]Intelligent Materials Solutions, Inc., Princeton, NJ 08540; [d]Optics Division, Athinoula A. Martinos Center for Biomedical Imaging, and [e]Neuroprotection Research Laboratory and Departments of Radiology and Neurology, Massachusetts General Hospital/Harvard Medical School, Charlestown, MA 02129

Edited by Timothy M. Swager, Massachusetts Institute of Technology, Cambridge, MA, and approved November 7, 2012 (received for review August 1, 2012)

We report a group of optical imaging probes, comprising upconverting lanthanide nanoparticles (UCNPs) and polyanionic dendrimers. Dendrimers with rigid cores and multiple carboxylate groups at the periphery are able to tightly bind to surfaces of UCNPs pretreated with $NOBF_4$, yielding stable, water-soluble, biocompatible nanomaterials. Unlike conventional linear polymers, dendrimers adhere to UCNPs by donating only a fraction of their peripheral groups to the UCNP–surface interactions. The remaining termini make up an interface between the nanoparticle and the aqueous phase, enhancing solubility and offering multiple possibilities for subsequent modification. Using optical probes as dendrimer cores makes it possible to couple the UCNPs signal to analyte-sensitive detection via UCNP-to-chromophore excitation energy transfer (EET). As an example, we demonstrate that UCNPs modified with porphyrin–dendrimers can operate as upconverting ratiometric pH nanosensors. Dendritic UCNPs possess excellent photostability, solubility, and biocompatibility, which make them directly suitable for in vivo imaging. Polyglutamic dendritic UCNPs injected in the blood of a mouse allowed mapping of the cortical vasculature down to 400 μm under the tissue surface, thus demonstrating feasibility of in vivo high-resolution two-photon microscopy with continuous wave (CW) excitation sources. Dendrimerization as a method of solubilization of UCNPs opens up numerous possibilities for use of these unique agents in biological imaging and sensing.

The role of optical-imaging methods in studying biological function through dynamic visualization of processes in tissues and cells cannot be overstated. The majority of optical techniques rely on luminescent probes, which, today, comprise a vast array of synthetic dyes and imaging nanoparticles and a large selection of fluorescent proteins. Nonetheless, the development of new contrast agents is still at the forefront of the imaging field, aiming to increase resolution, imaging speed, and analyte selectivity.

One active area of probe-development research is concerned with upconverting lanthanide-based nanoparticles (UCNPs) (1–3). The key property of these materials is their exceptional ability to upconvert near-infrared radiation into higher-energy light, offering numerous advantages of nonlinear excitation for biomedical imaging, such as lack of background fluorescence, increased tissue penetration for depth-resolved imaging, and reduced risk for photodamage.

Multiphoton sensitization in UCNPs (4) occurs via stepwise population of real long-lived states of lanthanide ions (5), in contrast to "virtual" states, involved in coherent two-photon absorption of conventional chromophores (6). Consequently, UCNPs possess extremely large apparent multiphoton absorption cross-sections (4), such that their emission can be readily induced by low-power continuous wave (CW) sources. Importantly, despite the differences in mechanisms, excitation of UCNPs still occurs in a nonlinear regime, laying ground for applications in multiphoton imaging (7).

Usefulness of UCNPs in optical detection has been demonstrated in a variety of biological settings, including analytical assays (8–10); imaging at the cellular (11–13), tissue, and organ levels (14–18); potential uses in optical tomography (19); single-particle detection (20); and multimodality imaging (21, 22). Success in the development and implementation of these techniques relies on one common requirement: availability of water-soluble, biologically compatible imaging probes. Conversely, UCNPs are commonly produced as complexes with hydrophobic capping ligands (23–26), which later must be replaced by hydrophilic shells. Efforts toward obtaining water-soluble nanoparticles encompass exchange of the capping ligands for various macromolecules (27, 28), encapsulation into SiO_2 layers and their subsequent modification (29–31), as well as wrapping of hydrophobic UCNPs with amphiphilic polymers (32). Overall, despite the significant progress, suboptimal stability of hydrophilic UCNPs still presents a major problem. For example, in many cases, initially low-scattering colloidal UCNP solutions form precipitates over time, presumably because of gradual desorption of ligands from nanoparticle surfaces and subsequent aggregation. Although for in vitro imaging, such semisoluble materials might be useful, in vivo applications require stable, well-soluble probes to avoid toxicity.

Here, we present an approach to solubilization of UCNPs based on noncovalent modification of their surfaces with polyanionic dendrimers. Our method capitalizes on multivalency, inherent to all dendrimers (33, 34), and the ability of some dendrimers to retain pseudoglobular shape even when they are bound to nanoparticle surfaces (35). UCNP/dendrimers exhibit excellent solubility and stability, reveal no apparent toxicity and, thus, can be used directly in vivo as multiphoton-imaging probes for high-resolution microscopy with low-power CW excitation sources. In addition, the ability to use optically active motifs as dendrimer cores enables coupling of UCNP emission to analyte-sensitive detection, charting a route to upconverting nanosensors for a variety of biological analytes.

Results and Discussion

Design Rationale. An ideal solubilizing jacket for a nanoparticle should comprise a ligand or a set of ligands that can adhere to its surface with high affinity, while keeping a sufficient number of hydrophilic groups exposed to the solvent (36). When molecules with one or a few surface-bound groups are used as surfactants, the binding affinity is determined by the energy of a single contact, making desorption a likely scenario. Cooperative binding is a straightforward way to enhance the binding energy, whereby multiple groups on a single ligand interact with the surface. In nanoparticle chemistry, this strategy is frequently implemented using polymer coatings, such as polyethyleneimine or polyacrylic

Author contributions: C.B.M. and S.A.V. designed research; T.V.E., X.Y., J.E.C., S.S., E.T.M., and S.A.V. performed research; T.V.E., X.Y., S.S., and S.A.V. analyzed data; and T.V.E. and S.A.V. wrote the paper.

The authors declare no conflict of interest.

This article is a PNAS Direct Submission.

[1]To whom correspondence may be addressed. E-mail: cbmurray@sas.upenn.edu or vinograd@mail.med.upenn.edu.

This article contains supporting information online at www.pnas.org/lookup/suppl/doi:10.1073/pnas.1213291110/-/DCSupplemental.

acid (PAA) (36). However, flexible polyfunctional polymers can easily adopt conformations in which virtually all of their groups are bound to the surface and just a few remain in contact with the solvent. As a result, the ligand–nanoparticle contacts strengthen, but the overall solubility does not improve significantly. In contrast, if a multivalent ligand is forced to retain globular shape, it will bind to the surface like a tennis ball to a Velcro-coated pad, leaving many groups in contact with the solvent and improving solubility.

Dendritic macromolecules present a natural choice of globular ligands with multiple peripheral functionalities (33, 34), warranting applications in nanoparticle chemistry (10, 37–39). Dendrimers are composed of identical branched motifs, dendrons, linked by their focal points to a single core unit. Suitably positioned anchor groups direct dendrons away from the core; however, when provided sufficient spatial freedom, flexible branches can fold back, yielding conformations in which most of the termini are grouped in the same spatial region, ready to bind to the surface. In contrast, dendrimers with rigid cores and many anchor points are more prone to keeping globular shape because of peripheral crowding (33), which occurs in these dendrimers already at early dendritic generations. We reasoned that such shape-persistent dendrimers should be superior to flexible polymers for the purpose of nanoparticle solubilization.

Polyglutamic Dendrimers. To functionalize UCNPs, we chose to use polyglutamic dendrimers, which exhibit very high aqueous solubility throughout physiological pH range, have excellent biocompatibility, and lack toxicity, as evidenced by numerous studies using them as in vivo oxygen probes (40, 41). In contrast, popular commercial amino-terminated dendrimers are less hydrophilic and may induce toxicity (42).

To facilitate formation of globular structures, we selected tetra-*meso*-3,5-dialkoxyarylporphyrin (**P**) as our initial core fragment (Fig. 1*A*). *meso*-aryl substituents in **P** are rotated ~73° relative to the tetrapyrrolic macrocycle (*SI Appendix*, *II. Calculations*), directing eight anchor groups above and below its plane. Generation (Gen) 4 polyglutamic dendrons (Fig. 1*G*) are capable of complete encapsulation of the core porphyrin, giving pseudoglobular dendrimers ~3.9 nm in diameter (*SI Appendix*, Fig. S1). Conversely, conformations in which all peripheral carboxylates point to the same direction, capable of binding to a surface, are energetically unfavorable.

Porphyrins possess strong visible absorption bands, which overlap with emission of Er^{3+}-doped UCNPs. This property turned out to be extremely useful in designing upconverting pH nanosensors (*vide infra*). However, to construct imaging probes, we chose dendrimers with equally rigid but noncolored core **C1** (Fig. 1*B*), dimension-wise resembling tetraarylporphyrins. In relaxed **C1**, peripheral aryls are tilted ~25° relative to the central benzene ring; however, the conformation in which all four aryls are orthogonal to the central ring is only 5.2 kcal/mol higher in energy (*SI Appendix*, *II. Calculations*). Upon decoration with bulky dendrons, these aryls are expected to rotate, facilitating formation of pseudoglobular structures (*SI Appendix*, Fig. S2). Use of the γ-aminobutyrate extension arms in **C1** (Fig. 1*B*) was essential for increasing the core solubility, as well as improving the yield of coupling reactions.

In addition to **P** and **C1**, 1,3,5-benzenetricarboxylic acid (**C2**) (Fig. 1*C*) was used in this study for comparison. **C2** has only three anchor groups, and, in Gen 4 **C2**–dendrimers, peripheral crowding should be much less pronounced. Therefore, **C2**–dendrimers may be expected to bind to UCNPs by engaging most of their carboxylates into surface interactions (*SI Appendix*, Fig. S3).

Gen 3 and 4 polyglutamic dendrons (Glu^3 and Glu^4) (Fig. 1*G*) were synthesized by the convergent method from *N-tert*-butoxycarbonyl protected L-glutamic acid and diethyl L-glutamate, using standard peptide coupling/deprotection chemistry (*SI Appendix*, *I. Synthesis*). Decoration of **P**, **C1**, and **C2** with the Glu dendrons after hydrolysis (which may have led to partial racemization) gave highly monodisperse water-soluble dendrimers **P**-Glu^4, **C1**-Glu^3, **C1**-Glu^4, and **C2**-Glu^4 with 128, 64, 128, and 48 peripheral carboxylates, respectively. Purity of the compounds was confirmed by MALDI-TOF and NMR analysis.

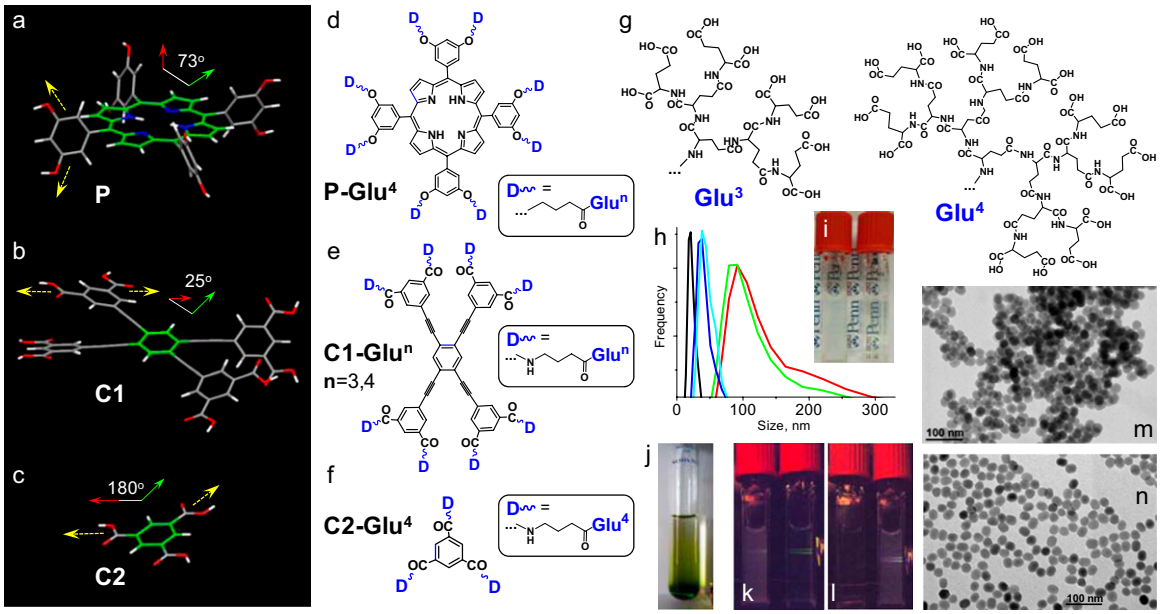

Fig. 1. (*A–C*) Structures of cores **P** (eight anchor groups), **C1** (eight anchor groups), and **C2** (three anchor groups) used for construction of dendrimers. Dihedral angles show orientation of the planes containing anchor groups relative to the core. (*D–F*) Polyglutamic dendrimers **P**-Glu^4 (128 carboxyls), **C1**-Glu^3 (64 carboxyls), **C1**-Glu^4 (128 carboxyls), and **C2**-Glu^4 (48 carboxyls). (*G*) Polyglutamic dendrons Glu^3 and Glu^4. (*H*) Size distributions of UCNP/dendrimers in aqueous solutions by DLS: UCNP/**C1**-Glu^3 (blue), UCNP/**C1**-Glu^4 (cyan), UCNP/**C2**-Glu^4 (red), UCNP/PAA (green), and UCNP/UCNP-BF_4^- in DMF (black). (*I*) Vials with aqueous colloidal solutions of UCNP/PAA (*Left*) and UCNP/**C1**-Glu^4 (*Right*) containing equal amounts of the inorganic material (20 mg/mL). (*J*) Gel formed upon centrifugation of UCNP/**P**-Glu^4. A hand-held laser pointer (980 nm) generates a green luminescent trace (near the bottom of the tube). (*K*) A laser beam (980 nm) passing through a solution of UCNP/**C1**-Glu^4 is able to excite luminescence of UCNP/**C2**-Glu^4 in the vial behind. (*L*) The order of vials is changed. The beam now is strongly scattered by UCNP/**C2**-Glu^4, and no luminescence of UCNP/**C1**-Glu^4 can be seen. (*M*) TEM image of UCNP/PAA. (*N*) TEM image of UCNP/**C1**-Glu^4.

UCNP Synthesis and Surface Modification. Synthesis of core nanoparticles and efficient procedure for removal of the primary hydrophobic capping layer is a prerequisite for obtaining hydrophilic UCNPs. We used hexagonal phase β-$NaYF_4$–based nanocrystals, doped with Yb^{3+} (20%) and Er^{3+} (2%) (43), which comprise one of the brightest known upconverting materials. Highly monodisperse spherical nanoparticles, 23 ± 1 nm in diameter, were prepared by thermal decomposition of trifluoroacetate salts in the presence of oleic acid (44). The oleate capping ligands were removed via the treatment with $NOBF_4$, rendering UCNPs coordinated by BF_4^- ions. The latter can readily undergo exchange reactions with a variety of ligands (e.g., PAA) (45). Importantly, no heating is required for completion of these steps, thus permitting use of even labile organic molecules for UCNP modification.

The nanoparticles were dendrimerized by simple mixing of dimethylformamide (DMF) solutions of UCNP-BF_4^- with aqueous solutions of dendrimers at room temperature. For comparison, UCNPs were also modified with PAA (average molecular mass, 1,800 Da), a common ligand for nanoparticle solubilization. Right after mixing, all solutions appeared optically clear, but upon centrifugation, which was necessary to remove DMF and unreacted ligands, UCNP/**C1**-Glu^3 and UCNP/**C1**-Glu^4 produced pale yellow soluble gels, whereas UCNP/PAA and UCNP/**G2**-Glu^4 precipitated as dense residues. Attempts to redissolve these precipitates (Fig. 1*I*) gave milky suspensions. UCNP/**P**-Glu^4 also gave a soluble gel, albeit dark green in color (Fig. 1*J*).

Aqueous solutions of UCNP adducts with **C1**-Glu^3, **C1**-Glu^4, and **P**-Glu^4 were found to be stable at pH 5–12 at 22 °C and could be stored for months at high concentrations (~200 mg/mL) or directly as gels without noticeable degradation. Remarkably, UCNP/**P**-Glu^4 was stored for over 1 y in solution (20 mg/mL), with no detectable loss of transparency. Acidification of UCNP/dendrimer solutions to pH 3–4 led to a slurry-like appearance but could be reversed back to transparency upon increase in pH. Drying of all of the above materials led to irreversible loss of solubility.

Properties of UCNP/Dendrimers. Differences between UCNPs modified by different ligands are immediately apparent in their scattering spectra (*SI Appendix*, Figs. S4 and S6) and can be detected easily by the naked eye (Fig. 1 *I*, *K*, and *L*), for example, by looking at luminescent traces produced by excitation with a handheld laser. A beam passing through a solution of UCNP/**C1**-Glu^4 (Fig. 1*K*) was scattered only weakly and retained enough power to excite UCNP/**C2**-Glu^4 in a cuvette placed behind. However, when the order of the samples was switched, no luminescence of UCNP/**C1**-Glu^4 was detectable because of the strong scattering by UCNP/**C2**-Glu^4.

Dynamic light scattering (DLS) (Fig. 1*H*) provided insight into the solution properties of the UCNP/dendrimers. Consistent with the presence of individual nonaggregated nanoparticles, UCNP/**C1**-Glu^3 and UCNP/**C1**-Glu^4 (20 mg/mL) exhibit narrow size distributions, centered near 35–40 nm. These species are larger than original UCNPs (~23 nm in DMF), presumably because of hydrated dendritic coats, but smaller than interparticle aggregates, which would be expected to show sizes at least twice the diameter of individual nanoparticles. In contrast, UCNP/**C2**-Glu^4 and UCNP/PAA reveal broad size distributions with maxima near 120 and 100 nm, respectively.

Transmission electron microscopy (TEM) (Fig. 1 *M* and *N* and *SI Appendix*, *V. Transmission Electron Microscopy*) shows the same aggregation trends in the solid state as seen in solutions. For example, UCNP/**C1**-Glu^4 (Fig. 1*N*) emerges in TEM images as individual nanoparticles, whereas images of UCNP/PAA (Fig. 1*M*) show chunks of aggregated material.

The number density of ligand molecules per UCNP was calculated based on the elemental analysis (*SI Appendix*, *III. Elemental analysis*). In all cases, surfaces of UCNPs appear to be densely covered by the ligands; and the total number of carboxylate groups per nanoparticle is nearly the same for all ligand types (~12,000). At the same time, experiments (above) clearly show that UCNPs modified with **C1**-Glu^3, **C1**-Glu^4, and **P**-Glu^4 exhibit much better solubility than those covered with **C2**-Glu^4 and PAA. This result suggests that it is not the total number of carboxylates but rather the ratio between bound and unbound carboxylate groups that governs the solubility. It follows that the fraction of the surface-bound carboxylates must be different between different ligand molecules. We hypothesize that this fraction depends on the shape that a molecule adopts upon binding to the surface.

To examine this hypothesis, we performed molecular simulations (*SI Appendix*, *II. Calculations* and Fig. S3*A*), which revealed that a linear molecule (PAA) can indeed easily adopt conformations in which over 60% of carboxylates become surface-bound. Likewise, dendrimer **C2**-Glu^4, possessing small trifunctional core, can flatten on the surface and donate 60–65% of its termini to the surface interactions. However, **C1**-Glu^3, having almost the same number of carboxylates as **C2**-Glu^4 but a rigid octa-functionalized core, is able to engage only ~18% of its carboxylates with the surface, while retaining ~72% interacting with solvent.

Combining these results with estimated surface coverage (from the elemental analysis), we can deduce that the larger solubilizing capacity of, for example, **C1**-Glu^4 comes from as many as ~10,200 free carboxylates per nanoparticle, making up the interface with the solvent, whereas in the case of UCNP/**C2**-Glu^4, this number is significantly less (*ca.* 4,300). Thus, the dendrimer core appears to play an important role in defining the solubilizing capacity.

Except for UCNP/**P**-Glu^4, the absorption spectra of UCNP/dendrimers in the visible region are dominated by scattering, but in addition, they show a characteristic Yb^{3+} band (λ_{max} = 977 nm). Excitation into this band induces upconverted emission, which resembles that of nondendrimerized UCNPs (Fig. 2*A*). The three main visible bands (λ_{max} = 527 nm, λ_{max} = 539 nm, and λ_{max} = 653 nm) correspond to the radiative transitions of Er^{3+} ion ($^2H_{11/2}\rightarrow{}^4I_{15/2}$, $^4S_{3/2}\rightarrow{}^4I_{15/2}$, and $^4F_{9/2}\rightarrow{}^4I_{15/2}$). The second order of excitation was confirmed by recording power dependencies of emission intensities (Fig. 2*B*). Compared with the UCNP-BF_4 in DMF, the green-to-red emission ratio in UCNP/dendrimers appears to be attenuated (Fig. 2*A*), suggesting stronger quenching of the $^2H_{11/2}$ and $^4S_{3/2}$ states by organic ligands and/or water molecules. Nevertheless, the red ($^4F_{9/2}\rightarrow{}^4I_{15/2}$) emission band remained almost unchanged. This band is most critical for biological imaging, because red light is much less absorbed by endogenous chromophores.

In Vivo Depth-Resolved Microscopic Imaging. Two-photon laser-scanning microscopy (2P LSM) (46) is one of today's tools of choice for functional physiological imaging with submicron resolution. Multiphoton excitation offers several advantages over linear methods, such as improved depth resolution and reduced risk for photodamage (7). However, 2P LSM typically requires extremely high local fluxes to compensate for generally low two-photon absorption cross-sections of fluorescent chromophores. Such fluxes are attainable through the use of expensive pulsed femtosecond lasers, which dramatically increase costs associated with this imaging method. Given that emission of UCNP/dendrimers can be induced by inexpensive CW lasers, we designed our experiments to compare the performance of UCNP/**C1**-Glu^4 in in vivo two-photon microscopy of mouse cerebral vasculature against regular vascular fluorescent probes.

First, a solution of dextran-conjugated fluorescein was injected into the mouse vasculature, the laser was mode-locked at 800 nm, and a stack of 200 images (512 × 512 pixels) spanning depths from 0 to 400 μm was acquired. The dwell time was 4 μs per pixel. The resulting maximum intensity projection (MIP) image of a 200-μm-thick upper portion of the stack (Fig. 3*C*) depicts a section of the vascular bed of the brain cortex. At a 10-mW average power, the peak pulse power in these experiments was ~1.25×10^3 W, corresponding to the photon flux of ~5.0×10^{27} photons per second per square centimeter in the beam focus (~1 μm in diameter).

Secondly, we lowered the power of the laser pump and turned off active mode-locking, converting the Ti:sapphire into a CW source. Several image planes were scanned at both 800- and 980-

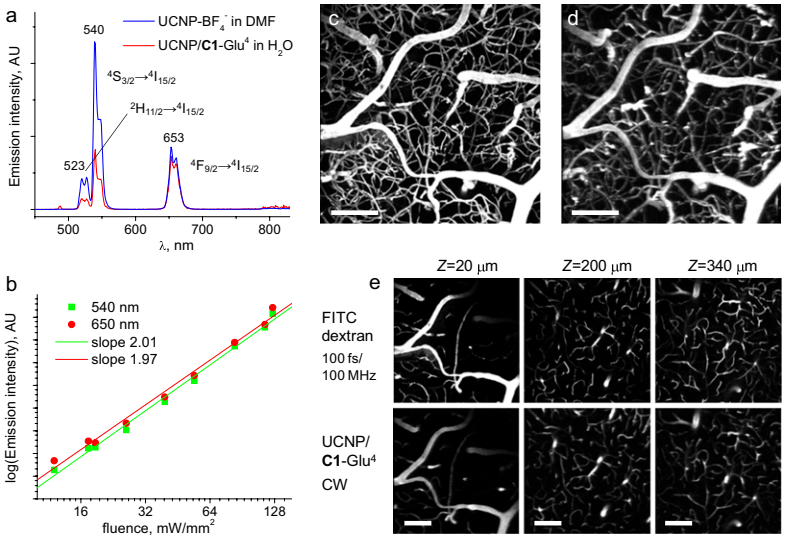

Fig. 2. (*A*) Emission of UCNP-BF_4^- in DMF and UCNP/**C1**-Glu^4 (in H_2O) induced by CW excitation at 980 nm. The samples contain equal amounts (by weight) of inorganic UCNPs. (*B*) Dependence of emission intensity at 540 and 650 nm for UCNP/**C1**-Glu^4 on the incident power (log–log plot). A nonfocused beam (1.5 mm in diameter) was used in this experiment (see *SI Appendix* for details). (*C*–*E*) Mouse brain imaging. (*C*) Maximal intensity projection (MIP) image of a 200-μm-thick image stack, from the surface down, acquired using FITC–dextran and a mode-locked Ti:sapphire laser (100 fs; 80-MHz repetition rate; 800-nm excitation wavelength). (*D*) MIP image of the same stack obtained with UCNP/**C1**-Glu^4 and the same laser operating in CW mode at 980 nm. (*E*) MIP images acquired at different depth. Stacks extend 20 μm down from the level marked above. (Scale bars: 100 μm.)

nm wavelengths, showing complete absence of emission, consistent with inability to excite FITC fluorescence in a two-photon regime at low photon fluxes.

A solution of UCNP/**C1**-Glu^4 (50 μL; 200 mg/mL) was then injected into the mouse blood (final concentration, ~3.3 mg/mL), and the same stack of images (0–400 μm) was scanned using 980 nm for excitation. Remarkably, the 3D contrast was fully regained (Fig. 3*D*), and the images appeared to match those obtained with FITC at all imaging depths, albeit the laser now operated in CW mode. The pixel dwell time was increased up to 20 μs to avoid smearing in the scanning direction attributable to the long emission lifetimes of UCNPs (Fig. 4*E*). Smearing at high scan speeds can be reduced by using confocal pinholes (12); however, this leads to rejection of a large portion of valuable signal. Importantly, the excitation power was kept as low as 1.5–1.7 mW (i.e., $\sim 8 \times 10^5$ times lower than the peak power in the pulsed operation), resulting in the flux of only $\sim 7.4 \times 10^{21}$ photons per second per square centimeter through the same focal cross-section.

No obvious signs of toxicity could be observed upon intravascular administration of UCNPs. During the entire imaging procedure, the heart rate and blood pressure of the mouse remained normal. As the acquisition progressed, the signal gradually faded as the probe was removed from the circulation, presumably because of the uptake by the liver and/or excretion through the kidneys. To maintain adequate signal, we administered additional 50 μL of the probe solution. Neither that nor the previous injection showed any effect on the physiological status of the animal. An additional four mice were tested by injecting similar probe doses, also not showing any signs of toxicity. The behavior of the animals on the following day appeared normal. Based on these observations, we conclude that UCNP/**C1**-Glu^4 can be safely used as a vascular multiphoton probe.

Previous attempts to use UCNP-based materials in tissue multiphoton microscopy were either performed in wide field, and, thus, did not achieve depth resolution (14), or required substitution of the entire blood volume with solution of imaging nanoparticles to attain adequate signal levels (18), thus not occurring truly in vivo. Despite large loads of the probe, the reported scan speeds (e.g., 200 μs per pixel) and resolution (e.g., 25 μm in Z) (18) were significantly lower than typically achieved in two-photon microscopy (7). In contrast, UCNP/dendrimers made it possible to perform truly in vivo depth-resolved, high-resolution imaging with CW sources at adequate scan rates and probe concentrations.

Excitation Energy Transfer: Application in pH Sensing. Excitation energy transfer (EET) from UCNPs to auxiliary chromophores provides a convenient way of coupling upconversion to various functions performed by these chromophores (9). For example, upconversion/EET has been used to quantify interactions of functionalized UCNPs with binding partners (10), shift emission wavelength for deeper tissue imaging (14, 17), and construct upconverting singlet oxygen sensitizers (47) and solid-state sensors (48). When the core of a dendrimer attached to the UCNP surface can perform simultaneously as an optical probe for a specific analyte, UCNP-to-dendrimer EET should enable analyte sensing via upconverted luminescence, whereby UCNPs play the role of low-flux multiphoton antennae in contrast to high-flux sensitization in dendritic systems with conventional antenna chromophores (49–51).

Polyglutamic porphyrin–dendrimers have been shown in the past to operate as efficient probes for pH in microheterogeneous systems (52). Porphyrin spectra undergo dramatic changes upon protonation (Fig. 3 *A* and *B*). Q_{11} band ($\lambda_{max} = 520$ nm) of free-base porphyrin (H_2P) overlaps with $^2H_{11/2} \rightarrow {}^4I_{15/2}$ emission of Er^{3+} ion (Fig. 3*E*), whereas Q_{00} band of the porphyrin dication H_4P^{2+} ($\lambda_{max} \sim 660$ nm) overlaps with $^4F_{9/2} \rightarrow {}^4I_{15/2}$ emission band (Fig. 3*C*). Porphyrin transitions have large oscillator strengths, thereby acting as acceptors of UCNP luminescence, so that the green and red emission bands are attenuated differently depending on the protonation state of the porphyrin (Fig. 3*D*). By exciting UCNP/**P**-Glu^4 near 980 nm and rationing the visible UCNP emission bands, a ratiometric protonation curve can be constructed.

To demonstrate this principle (Fig. 3 *D* and *E*), small portions of aqueous HCl were added to a solution of UCNP/**P**-Glu^4, which led to a gradual change in the red/green emission ratio. The resulting sigmoidal plot (Fig. 3*E*) provides an analytical curve for pH, whereby the signal is obtained via multiphoton upconversion. One key advantage of this sensing approach is that the probe itself (porphyrin in our case) does not have to be emissive, which greatly expands the selection of potential sensing chromophores. Secondly, the scheme can be extended on virtually any analyte as long as the optical transitions of the chromophore overlaps with emission bands of UCNP. Compared with conventional macromolecular pH probes [e.g., seminaphthorhodafluor (SNARF)–dextrans; Invitrogen], UCNPs can be excited by low-power near-infrared sources. For example, upon direct injection into the tissue interstitial space, UCNP/dendrimers may be used for mapping of pH in hypoxic tumors, including high-resolution two-photon microscopic measurements.

Time-resolved emission intensity profiles ($\lambda_{em} = 660$ nm) were recorded at three different pH values upon excitation of UCNP/**P**-Glu^4 using 980-nm laser pulses (Fig. 3*H*). The curves comprise characteristic rise and decay phases, corresponding to the sensitization and subsequent decay of the Er^{3+}-excited state. The decay lifetimes (τ_d) appear to only weakly depend of pH, whereas the integrated intensity of the red transition decreases *ca.* 40% from

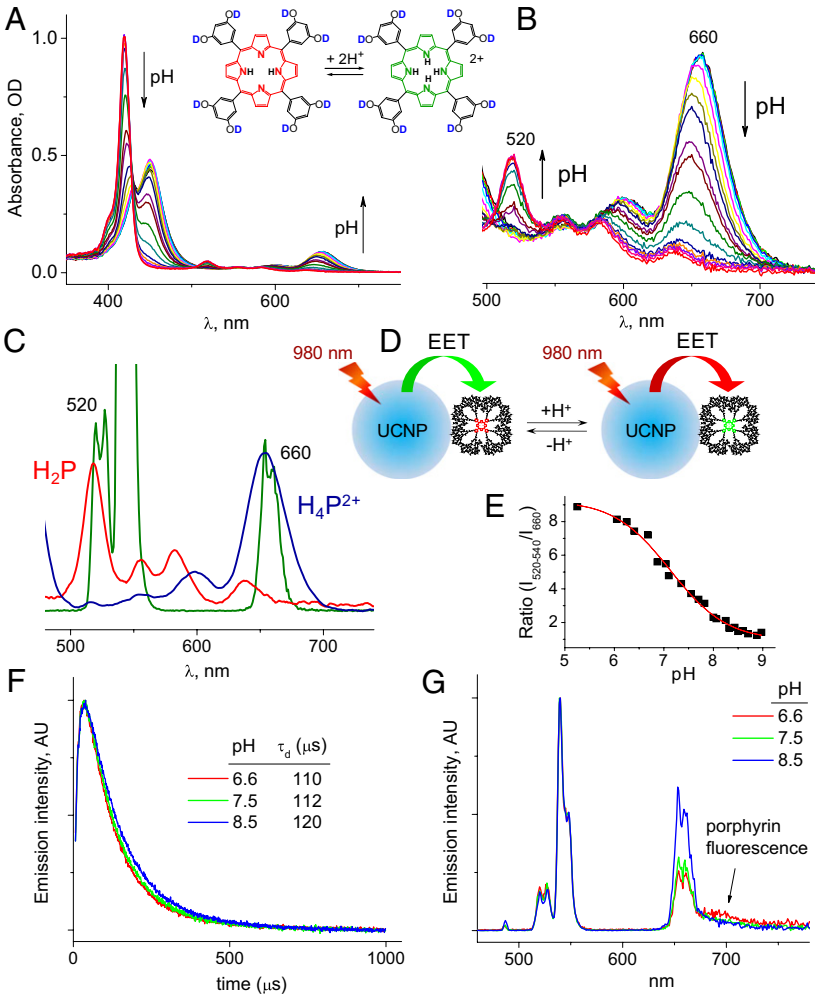

Fig. 3. (*A* and *B*) Changes in the absorption spectra of porphyrin–dendrimer **P**-Glu^4 with change in pH. (*C*) Q bands of free-base porphyrin H_2P (red) and porphyrin dication H_4P^{2+} (blue) overlap with emission bands of UCNP. (*D*) Cartoon illustrating pH sensing by UCNP/**P**-Glu^4 via upconversion and EET. (*E*) pH-titration curve obtained by rationing integrated intensities of UCNP/**P**-Glu^4 transitions at 520–540 nm and 660 nm (λ_{ex} = 980 nm). (*F*) Time-resolved emission traces of UCNP/**P**-Glu^4 at 660 nm recorded upon pulsed excitation at 980 nm at three different pH levels. (*G*) Steady-state emission spectra for the same three samples.

basic (least overlap with porphyrin) to acidic (most overlap with porphyrin) state (Fig. 3*J*). This result suggests that the EET in the UCNP/**P**-Glu^4 system occurs predominantly via the "trivial" emission–reabsorption mechanism, whereas only a small fraction of the energy is transferred by way of non–radiative-type interaction. Indeed, in the case of a nonradiative mechanism, UCNP decay lifetimes would be scaled proportionally to the integrated intensities. Emission–reabsorption is consistent with rather large separation between the emitting ions within the nanocrystal lattice and the surface-adhered porphyrin–dendrimers.

The fluorescence quantum yield of the porphyrin (pH 9) of UCNP/**P**-Glu^4 was found to be nearly the same as that of free **P**-Glu^4 in solution ($\phi_{fl} \approx 0.025$), whereas the shifts in the absorption and emission spectra of the porphyrin in UCNP/**P**-Glu^4 indicate interaction between the dendrimer, nanoparticle surface, and possibly other neighboring dendrimers. A change in the intensity of a shoulder near 700 nm (Fig. 3*J*), occurring with change in pH, suggests that this emission originates from the porphyrin and is excited via upconversion. It will be interesting to explore in the future the utility of this secondary signal.

Conclusions

In conclusion, we reported dendrimerization as an efficient ligand-exchange method leading to soluble upconverting nanoparticles for multiphoton imaging and sensing. By using dendrimers with optically active cores, UCNPs can be transformed into upconverting ratiometric sensors for specific analytes, such as pH. Excellent solubility and lack of apparent toxicity of dendritic UCNPs enabled in vivo depth-resolved, high-resolution imaging of tissue with CW laser sources using photon fluxes almost 10^6 times lower that typically used in two-photon imaging.

Materials and Methods

All solvents and reagents were purchased from commercial sources and used as received. UCNPs were synthesized as described previously (28). For synthesis and characterization of dendrimers and UCNP/dendrimers, see *SI Appendix*.

^{1}H and ^{13}C NMR spectra were recorded on a Bruker DPX-400 spectrometer operating at 400.1 or 100.6 MHz, respectively. Mass spectra were recorded on a MALDI-TOF Bruker Daltonics Microflex LRF instrument, using α-cyano-4-hydroxycinnamic acid (CCA) as a matrix in positive-ion mode. Optical spectra were recorded on a Perkin-Elmer Lambda 35 UV-Vis spectrometer. Steady-state luminescence measurements were performed on FS920 spectrofluorometer (Edinburgh Instruments), equipped with an R2658P photomultiplier (PMT) (Hamamatsu). Quartz fluorometric cells (1-cm path length; Starna) were used in optical experiments. DLS measurements were carried out on a Zetasizer NanoS instrument (Malvern). TEM images were acquired on a JEM-1400 microscope (Jeol) using a 120-kV accelerating voltage. Details of calculations, pH titrations, and elemental analysis are given in *SI Appendix*.

The fluorescence quantum yields of **P**-Glu^4 and UCNP/**P**-Glu^4 were measured against fluorescence of Rhodamine 6G in EtOH (Φ_{fl} = 0.94) (53). Scattering spectra of UCNPs modified with dendritic ligands and PAA were obtained by synchronously scanning excitation and emission monochromators of the fluorometer while recording the corrected emission signal. For steady-state measurements of UCNP emission via upconversion, a compact CW laser diode (λ_{max} = 980 nm) was placed inside the fluorometer and used as an excitation source. The beam of the diode was directed at the optical cell at the right angle relative to the detector. A short-pass filter (900-nm cutoff; Asahi Spectra) was inserted into the emission path. Emission spectra were corrected by response curve of the PMT. For power-dependence measurements, the

incident power on the sample was varied by using neutral density filters and measured by an optical power meter (Coherent). The beam was not focused in the power-dependence measurements.

Time-resolved measurements of emission via upconversion were performed using a setup for cellular two-photon phosphorescence lifetime microscopy described previously (54). In vivo imaging was performed in epi-fluorescence mode using a previously developed system (55), based on a commercial two-photon microscope (Ultima; Prairie Technologies). The excitation was provided by a Ti:sapphire oscillator (100-fs pulse width; 80-MHz repetition rate; Mai-Tai HP; Spectra Physics). Beam focusing and collection of emission were accomplished by a water-immersion lens (20×; NA 0.95; XLUMPLFI; Olympus). Three-dimensional median filter and histogram equalization were used for image processing.

For vascular imaging, C57BL mice (male; 25–30 g; 10–12 wk old) were anesthetized by isoflurane (1–2% in a mixture of O_2 and N_2O) under constant temperature (37 °C). A cranial window was made in the parietal bone, the dura was removed, and the window was sealed with a 150-μm-thick microscope coverslip. During imaging, blood pressure and blood gases were monitored via the catheter inserted into the femoral artery, which also served for administration of probes. All experimental procedures were approved by the Massachusetts General Hospital Subcommittee on Research Animal Care.

ACKNOWLEDGMENTS. This work was supported, in part, by the Nano/Bio Interface Center through National Science Foundation Nanoscale Science and Engineering Centers Grant DMR08-32802 (to S.A.V. and C.B.M.), the Penn Medicine Neuroscience Center grant (to S.A.V.), the Office of Naval Research Multidisciplinary University Research Initiative on Optical Metamaterials through Award N00014-10-1-0942 (to C.B.M.), American Heart Association Grant 11SDG7600037 (to S.S.), and Prairie Microscope Shared Instrument Equipment Grant S10-RR022428 from the National Institutes of Health.

1. Chatterjee DK, Rufaihah AJ, Zhang Y (2008) Upconversion fluorescence imaging of cells and small animals using lanthanide doped nanocrystals. *Biomaterials* 29(7):937–943.
2. Wang F, Banerjee D, Liu Y, Chen X, Liu X (2010) Upconversion nanoparticles in biological labeling, imaging, and therapy. *Analyst (Lond)* 135(8):1839–1854.
3. Zhou J, Liu Z, Li F (2012) Upconversion nanophosphors for small-animal imaging. *Chem Soc Rev* 41(3):1323–1349.
4. Auzel F (2004) Upconversion and anti-Stokes processes with f and d ions in solids. *Chem Rev* 104(1):139–173.
5. Ovsyakin VV, Feofilov PP (1966) Mechanism of summation of electronic excitations in activated crystals. *JETP Lett* 3(12):322–327.
6. Göeppert-Mayer M (1931) Über Elementarakte mit zwei Quantensprüngen. *Ann Phys* 9(3):273–295.
7. Zipfel WR, Williams RM, Webb WW (2003) Nonlinear magic: Multiphoton microscopy in the biosciences. *Nat Biotechnol* 21(11):1369–1377.
8. Zijlmans HJ, et al. (1999) Detection of cell and tissue surface antigens using up-converting phosphors: A new reporter technology. *Anal Biochem* 267(1):30–36.
9. Zhang P, Rogelj S, Nguyen K, Wheeler D (2006) Design of a highly sensitive and specific nucleotide sensor based on photon upconverting particles. *J Am Chem Soc* 128(38):12410–12411.
10. Bogdan N, Vetrone F, Roy R, Capobianco JA (2010) Carbohydrate-coated lanthanide-doped upconverting nanoparticles for lectin recognition. *J Mater Chem* 20(35):7543–7550.
11. Vetrone F, et al. (2010) Intracellular imaging of HeLa cells by non-functionalized $NaYF_4$: Er^{3+}, Yb^{3+} upconverting nanoparticles. *Nanoscale* 2(4):495–498.
12. Yu MX, et al. (2009) Laser scanning up-conversion luminescence microscopy for imaging cells labeled with rare-earth nanophosphors. *Anal Chem* 81(3):930–935.
13. Nyk M, Kumar R, Ohulchanskyy TY, Bergey EJ, Prasad PN (2008) High contrast in vitro and *in vivo* photoluminescence bioimaging using near infrared to near infrared upconversion in Tm^{3+} and Yb^{3+} doped fluoride nanophosphors. *Nano Lett* 8(11):3834–3838.
14. Hilderbrand SA, Shao FW, Salthouse C, Mahmood U, Weissleder R (2009) Upconverting luminescent nanomaterials: Application to in vivo bioimaging. *Chem Commun (Camb)* (28):4188–4190.
15. Xiong LQ, et al. (2009) High contrast upconversion luminescence targeted imaging *in vivo* using peptide-labeled nanophosphors. *Anal Chem* 81(21):8687–8694.
16. Kobayashi H, et al. (2009) *In vivo* multiple color lymphatic imaging using upconverting nanocrystals. *J Mater Chem* 19(36):6481–6484.
17. Cheng LA, Yang K, Shao MW, Lee ST, Liu ZA (2011) Multicolor *in vivo* imaging of upconversion nanopaticles with emissions tuned by luminescence resonance energy Transfer. *J Phys Chem C* 115(6):2686–2692.
18. Pichaandi J, Boyer JC, Delaney KR, van Veggel F (2011) Two-photon upconversion laser (scanning and wide-field) microscopy using Ln^{3+}-doped $NaYF_4$ upconverting nanocrystals: A critical evaluation of their performance and potential in bioimaging. *J Phys Chem C* 115(39):19054–19064.
19. Xu CT, Axelsson J, Andersson-Engels S (2009) Fluorescence diffuse optical tomography using upconverting nanoparticles. *Appl Phys Lett* 94(25):251107.
20. Wu S, et al. (2009) Non-blinking and photostable upconverted luminescence from single lanthanide-doped nanocrystals. *Proc Natl Acad Sci USA* 106(27):10917–10921.
21. Kumar R, Nyk M, Ohulchanskyy TY, Flask CA, Prasad PN (2009) Combined optical and MR bioimaging using rare earth ion doped $NaYF_4$ nanocrystals. *Adv Funct Mater* 19(6):853–859.
22. Park YI, et al. (2009) Nonblinking and nonbleaching upconverting nanoparticles as an optical imaging nanoprobe and T_1 magnetic resonance imaging contrast agent. *Adv Mater (Deerfield Beach Fla)* 21(44):4467–4471.
23. Mai HX, et al. (2006) High-quality sodium rare-earth fluoride nanocrystals: Controlled synthesis and optical properties. *J Am Chem Soc* 128(19):6426–6436.
24. Yi GS, Chow GM (2006) Synthesis of hexagonal-phase $NaYF_4$:Yb,Er and $NaYF_4$:Yb,Tm nanocrystals with efficient up-conversion fluorescence. *Adv Funct Mater* 16(18):2324–2329.
25. Chan EM, et al. (2010) Reproducible, high-throughput synthesis of colloidal nanocrystals for optimization in multidimensional parameter space. *Nano Lett* 10(5):1874–1885.
26. Wang F, et al. (2010) Simultaneous phase and size control of upconversion nanocrystals through lanthanide doping. *Nature* 463(7284):1061–1065.
27. Chen ZG, et al. (2008) Versatile synthesis strategy for carboxylic acid-functionalized upconverting nanophosphors as biological labels. *J Am Chem Soc* 130(10):3023–3029.
28. Boyer J-C, Manseau M-P, Murray JI, van Veggel FCJM (2010) Surface modification of upconverting $NaYF_4$ nanoparticles with PEG-phosphate ligands for NIR (800 nm) biolabeling within the biological window. *Langmuir* 26(2):1157–1164.
29. Li Z, Zhang Y (2006) Monodisperse silica-coated polyvinylpyrrolidone/$NaYF_4$ nanocrystals with multicolor upconversion fluorescence emission. *Angew Chem Int Ed* 45 (46):7732–7735.
30. Shan J, et al. (2008) Biofunctionalization, cytotoxicity, and cell uptake of lanthanide doped hydrophobically ligated $NaYF_4$ upconversion nanophosphors. *J Appl Phys* 104(9):094308.
31. Hu H, et al. (2009) Multimodal-luminescence core-shell nanocomposites for targeted imaging of tumor cells. *Chemistry* 15(14):3577–3584.
32. Cheng L, et al. (2010) Highly-sensitive multiplexed *in vivo* imaging using PEGylated upconversion nanoparticles. *Nano Research* 3(10):722–732.
33. Tomalia DA, Naylor AM, Goddard WA III (1990) Starburst dendrimers: Molecular-level control of size, shape,surface chemistry, topology, and flexibility from atoms to macroscopic matter. *Angew Chem Int Ed Engl* 29(2):138–175.
34. Newkome GR, Moorefield CN, Vogtle F (2001) *Dendrimers and Dendrons: Concepts, Syntheses, Applications* (Wiley-VCH, Weinheim).
35. Tully DC, Frechet JMJ (2001) Dendrimers at surfaces and interfaces: Chemistry and applications. *Chem Commun (Camb)* (14):1229–1239.
36. Zhang T, Ge J, Hu Y, Yin Y (2007) A general approach for transferring hydrophobic nanocrystals into water. *Nano Lett* 7(10):3203–3207.
37. Wisher AC, Bronstein I, Chechik V (2006) Thiolated PAMAM dendrimer-coated CdSe/ZnSe nanoparticles as protein transfection agents. *Chem Commun (Camb)* (15): 1637–1639.
38. Shi X, Thomas TP, Myc LA, Kotlyar A, Baker JR, Jr. (2007) Synthesis, characterization, and intracellular uptake of carboxyl-terminated poly(amidoamine) dendrimer-stabilized iron oxide nanoparticles. *Phys Chem Chem Phys* 9(42):5712–5720.
39. Shi X, et al. (2007) Dendrimer-entrapped gold nanoparticles as a platform for cancer-cell targeting and imaging. *Small* 3(7):1245–1252.
40. Vinogradov SA, Lo LW, Wilson DF (1999) Dendritic polyglutamic porphyrins: Probing porphyrin protection by oxygen-dependent quenching of phosphorescence. *Chemistry* 5(4):1338–1347.
41. Vinogradov SA, Wilson DF (2010) Porphyrin-dendrimers as biological oxygen sensors. *Designing Dendrimers*, eds Capagna S, Ceroni P (Wiley, New York), pp 463–503.
42. Jones CF, et al. (2012) Cationic PAMAM dendrimers disrupt key platelet functions. *Mol Pharm* 9(6):1599–1611.
43. Heer S, Kompe K, Gudel HU, Haase M (2004) Highly efficient multicolour upconversion emission in transparent colloids of lanthanide-doped $NaYF_4$ nanocrystals. *Adv Mater (Deerfield Beach Fla)* 16(23-24):2102–2108.
44. Ye X, et al. (2010) Morphologically controlled synthesis of colloidal upconversion nanophosphors and their shape-directed self-assembly. *Proc Natl Acad Sci USA* 107(52):22430–22435.
45. Dong AG, et al. (2011) A generalized ligand-exchange strategy enabling sequential surface functionalization of colloidal nanocrystals. *J Am Chem Soc* 133(4):998–1006.
46. Denk W, Strickler JH, Webb WW (1990) Two-photon laser scanning fluorescence microscopy. *Science* 248(4951):73–76.
47. Zhang P, Steelant W, Kumar M, Scholfield M (2007) Versatile photosensitizers for photodynamic therapy at infrared excitation. *J Am Chem Soc* 129(15):4526–4527.
48. Xie LX, Qin Y, Chen HY (2012) Polymeric optodes based on upconverting nanorods for fluorescent measurements of pH and metal ions in blood samples. *Anal Chem* 84(4): 1969–1974.
49. Dichtel WR, et al. (2004) Singlet oxygen generation via two-photon excited FRET. *J Am Chem Soc* 126(17):5380–5381.
50. Briñas RP, Troxler T, Hochstrasser RM, Vinogradov SA (2005) Phosphorescent oxygen sensor with dendritic protection and two-photon absorbing antenna. *J Am Chem Soc* 127(33):11851–11862.
51. Yan XZ, Goodson T, 3rd, Imaoka T, Yamamoto K (2005) Up-converted emission in a series of phenylazomethine dendrimers with a porphyrin core. *J Phys Chem B* 109(19):9321–9329.
52. Finikova OS, et al. (2003) Porphyrin and tetrabenzoporphyrin dendrimers: Tunable membrane-impermeable fluorescent pH nanosensors. *J Am Chem Soc* 125(16):4882–4893.
53. Kubin RF, Fletcher AN (1982) Fluorescence quantum yields of some rhodamine dyes. *J Lumin* 27(4):455–462.
54. Sinks LE, et al. (2010) Two-photon microscopy of oxygen: Polymersomes as probe carrier vehicles. *J Phys Chem B* 114(45):14373–14382.
55. Sakadzić S, et al. (2008) Multi-photon microscopy with a low-cost and highly efficient Cr:LiCAF laser. *Opt Express* 16(25):20848–20863.